



Synthesis and Computational Design of Dual-Targeting Thienopyrimidine Kinase Inhibitors: DFT Guided Optimization of Covalent EGFR/VEGFR2 Inhibition with Favorable Docking and ADMET Properties

Abdul Ghafoor

Department of Chemistry, University of Sahiwal, Sahiwal, Pakistan

Javeria Rasool

Department of Chemistry, University of Sahiwal, Sahiwal, Pakistan

Naved Sajid

Department of Chemistry, The Islamia University of Bahawalpur, Bahawalpur, Pakistan

Hibba Asghar

Department of Chemistry, University of Sahiwal, Sahiwal, Pakistan

Danish Ali

Department of Chemistry, The Islamia University of Bahawalpur, Bahawalpur, Pakistan

Hasba Fatima

Department of Chemistry, University of Sahiwal, Sahiwal, Pakistan

Shahzaib

Department of Chemistry, University of Sahiwal, Sahiwal, Pakistan

Amina Zara Chaudhary

Department of Chemistry, COMSATS University Islamabad, Lahore Campus and Department of Chemistry, University of Sahiwal, Sahiwal, Pakistan

Muhammad Amir Abbas

Department of Chemistry, Bahauddin Zakariya University Multan, Pakistan

Amin Abid

Department of Chemistry, University of Sahiwal, Sahiwal, Pakistan

ABSTRACT

In the present study we report the thienopyrimidine kinase inhibitors through integrated computational methods at DFT/B3LYP/6-31++G(d,p). Quantum chemical calculation and molecular docking was employed to explore reactivity and medicinal significance. Evaluation of two derivatives against CDK2, GSK-3 β , EGFR T790M, JAK2 V617F-JR-1, and VEGFR2 revealed that VEGFR2-JR-2 exhibited superior binding (-5.625 kcal/mole) *via* π -cation interactions with TRP531, supported by optimal HOMO localization (98% thienopyrimidine contribution) and favorable quantum descriptors HOMO-LUMO gap = 3.91 eV, electrophilicity = 1.38 eV). DFT-optimized structures identified the optimal warhead position (Fukui = 0.081) for EGFR inhibition. At the same time, GSK-3 β -JR-1 demonstrated enhanced hydrophobic complementarity (ΔE_{vdW} = -38.2 kcal/mole with PHE8) correlated with low chemical potential (μ = -3.72 eV). QM simulations confirmed charge transfer 0.32 to kinase hinge regions, and 100 ns MD trajectories validated covalent binding potential (CYS532-S C = 3.4 ± 0.2 Å). These results establish JR-2 as a promising anti-angiogenic lead compound and provide a quantum-validated estimations for developing next-generation thienopyrimidine kinase inhibitors.

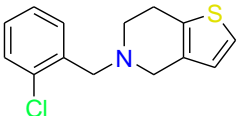
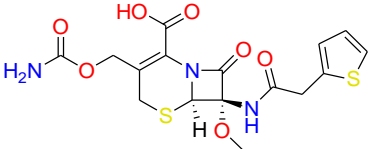
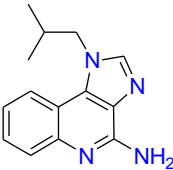
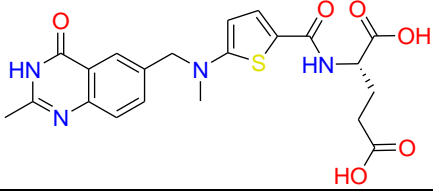

Keywords: Thienopyrimidine, Kinase Inhibitors, DFT Studies, Docking, ADMET.

INTRODUCTION

Heterocyclic compounds are a diverse class of organic compounds, characterized by the presence of a ring structure containing at least one heteroatom in addition to carbon atoms. These heterocyclic frameworks are widely distributed in both natural and synthetic sources and are well recognized for their broad range of pharmacological activities. Heterocyclic compounds are regarded as one of the most important classes of organic molecules, widely utilized in various biological fields for their activity against multiple diseases [1-6]. Nitrogen containing heterocycles are considered a vital class of compounds, widely represented in physiologically active complexes, natural products, and synthetic chemicals, and they play a pivotal role in medicinal chemistry [7-9]. Their favorable properties, such as enhanced solubility, polarity, and hydrogen bonding ability, make them attractive candidates for drug development. Nitrogen-bearing heterocycles, such as indole, [10] imidazole, [11] pyrrole, [12] triazole, [13] piperazine have acquire importance in many research sectors including synthesis and medicine [14-19]. In contrast, oxygen-containing heterocycles constitute a substantial proportion of FDA approved drugs and form the backbone of numerous therapeutically important structures [20]. The sulphur containing compounds like benzothiazole, thiophene have been proven to exert anticancer [21,22], antimicrobial [23], antiviral [24], anti-inflammatory [25] and many other biological activities. A wide range of FDA approved drugs incorporate nitrogen and sulfur-containing heterocycles, including well-known examples such as anastrozole, abemaciclib, tamoxifen, 5-fluorouracil, and clopidogrel (Table 1) are clinically approved drugs containing heterocyclic compounds used to cure breast cancer, diabetes and many other diseases [26-31]. Moreover, thienopyrimidine based compounds are widely represented in numerous pharmaceutical formulations [32] and as natural products [33]. Moreover, several studies have reported that thienopyrimidines can modulate melanin synthesis in murine B16 cells [34,35]. M. A. Mohamed *et al* the thienopyrimidine to their a cyclo-nucleosides regarded [36,37] as anti-cancer [38]. In light of the aforementioned findings and our growing interest in the chemistry of thieno[2,3-d]pyrimidines [38-41] Mona M. Abdel-Atty

et al despite the efficiency of HDAC inhibition as monotherapy in hematologic malignancies, it did not show significant competency against solid tumors. Consequently, multitarget therapy has emerged as a promising yet challenging strategy to enhance the efficacy of HDAC inhibitors [42]. The combination of HDAC inhibitors with tyrosine kinase inhibitors (TKIs) is regarded as a promising strategy to enhance therapeutic efficacy and overcome drug resistance. For instance, the combination of gefitinib (an EGFR inhibitor) with vorinostat (an HDAC inhibitor) has demonstrated a synergistic effect, resulting in greater tumor growth inhibition and enhanced apoptosis compared to monotherapy with selective EGFR inhibitors [43,44]. Despite their broad applicability, further investigation is required to fully elucidate the reactivity and bioinformatic characteristics of thienopyrimidines in drug development. In medicinal chemistry, addressing this gap is crucial for unlocking their complete therapeutic potential.

Table 1: Heterocyclic frameworks in clinically approved drugs

Drug	Structure	Clinical indication
Ticlopidine		Preventing certain cells in the blood from clumping together
Cefoxitin		Surgery to prevent infection
Imiquimod		Actinic keratosis, Basal cell carcinoma, Genital warts
Raltitrexed		leading to inhibition of DNA replication and apoptosis in rapidly proliferating cancer cells
Omeprazole		Used to gastroesophageal reflux disease

This study builds on previous advancements by concentrating on the fabrication of thienopyrimidine-derivatives namely. This study aimed to computationally explore the structural characteristics and binding interactions of these derivatives using DFT at B3LYP/6-31++G(d,p) level of theory. Standard spectroscopic methods, such as FTIR, UV-visible ^1H NMR, and ^{13}C NMR, were used to characterize the computed results with real-world reported data. In addition, non-covalent interactions (NCIs), HOMO-LUMO charge distribution, identification of electrophilic and nucleophilic regions was also articulated. In medicinal chemistry, Lipinski's rule of five, toxicity, and metabolic prediction was studies to understand the significance of these compounds. The biological activity of these compounds against four cancer-related

enzymes (PDB ID: CYP3A4, CYP2D6, CYP1A2, CYP2C9, CYP2C19) was assessed using a molecular docking to investigate their therapeutic potential.

EXPERIMENTAL

Chemicals and Solvents

All solvents used were laboratory grade and were dried over suitable drying agents when required or used without further purification. All aqueous solutions were prepared using Milli-Q water. Analytical thin-layer chromatography (TLC) was carried out on Merck Kieselgel 60 F254 precoated sheets (0.25 mm, 230–400 mesh). Flash column chromatography was performed on Kieselgel 60 silica (230–400 mesh) using the solvent systems specified. Greiner black polypropylene 96-well plates were used for plate reader measurements. Other reagents were purchased from Sigma Aldrich and Alfa Aesar. Commercial materials were used as received unless otherwise noted.

Analytical Methods and Instrumentations:

Infrared spectra were recorded on a Bruker ALPHA FT-IR (neat) and reported as max, the frequency of peak maxima in cm^{-1} . ^1H -NMR spectra were recorded at 300 K using Bruker DRX 300 at frequency of 300 MHz. The data are reported as a chemical shift in ppm, multiplicity, relative integral, and coupling constant (J) in Hz. Low resolution mass spectrometry was performed on a Finnegan LACS quadrupole ion trap mass spectrometer operating in positive ion mode with electrospray ionization (ESI) or atmospheric pressure chemical ionization. Fluorescence measurements were performed using a PerkinElmer EnSpire multimode plate reader.

Procedure

A blend of 5,6,7,8-tetrahydro[1]benzothieno[2,3-d]pyrimidin-4(3H)-one and POCl_3 was refluxed for 2 hours, and after cooling, it was poured into ice cold water. Acquired precipitates was filtered, washed with ethanol, and dried.

4-chloro-5,6,7,8 tetrahydro[1]benzothieno[2,3-d]pyrimidine (JR-1)

Color: cream colour powder, Yield: 51%, Melting point: 274°C , IR (neat) (cm^{-1}): 3408, 1682, 1587, 1529, 1232, ^1H NMR (300 MHz, DMSO-d_6): δ 7.97 (s, 1H), 2.91-2.82 (m, 2H), 2.78-2.67 (m, 2H), 1.85-1.69 (m, 4H), ^{13}C NMR (75 MHz, DMSO-d_6): δ 152.4, 155.7, 146.8, 130.1, 128.8, 118.7, 25.3, 24.4, 22.5, 21.8, MS (ESI): $[\text{M}+\text{H}]$ 205.1.

Procedure

2-amino-4,5,6,7-tetrahydro-1-benzothiophene-3-carbonitrile (0.01 mol) in formic acid (5mL) was refluxed with formamide (0.01 mol). The reaction mix was carried out for 2 hrs. and subsequently cooled to room temperature. Acquired precipitates were filtered, washed with ethanol, and dried.

5,6,7,8-tetrahydro[1]benzothieno[2,3-d]pyrimidin-4-amine (JR-2)

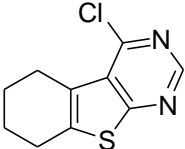
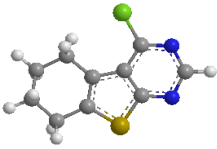
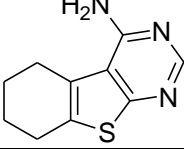
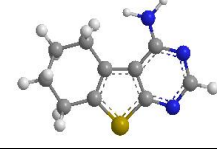
Color: cream colour powder, Yield: 51%, Melting point: 224°C , IR (cm^{-1}): 3171, 1665, 1578, 1388, 1292, 1165, ^1H NMR (300 MHz, $\text{CHCl}_3\text{-d}$): δ 7.19 (s, 3 H), 2.37 - 2.46 (m, 6 H), 1.95 - 2.33 (m, 2 H), 1.72 - 1.78 (m, 3 H), 1.44 - 1.67 (m, 2 H), 1.03 - 1.22 (m, 1 H). ^{13}C NMR (75 MHz, DMSO-d_6): δ 152.4, 155.7, 146.8, 130.1, 128.8, 118.7, 25.3, 24.4, 22.5, 21.8, MS (ESI): $[\text{M}+\text{H}]$ - 206.07.

COMPUTATIONAL METHODOLOGY

DFT calculations were performed using Gaussian 16 at the B3LYP/6-31++G(d,p) level of theory to optimize the molecular geometries of JR-1 and JR-2 and evaluate their electronic properties. The 6-31++G(d,p) basis set was selected for its balanced accuracy in describing both valence and polarization effects, particularly for systems containing heteroatoms (S or N) and potential hydrogen bonding interactions. Diffuse functions (++) were included to better capture electron density distribution in lone pairs and anionic regions, while polarization functions (d,p) ensured accurate treatment of bond polarization and molecular orbital hybridization. Frequency calculations confirmed the absence of imaginary vibrational modes, confirming that the optimized geometries correspond to true energy minima. Key electronic parameters, including frontier molecular orbitals (HOMO-LUMO gaps), Mulliken charges, and electrostatic potential (ESP) maps, were computed to assess reactivity and intermolecular interactions. The results provide a robust theoretical foundation for interpreting experimental structural data and predicting chemical behavior.

Based on our understanding of the available literature, no theoretical works have been reported pyridine-based derivatives. This is the first systematic investigation of novel and highly elongated pyridine-based derivatives. In the context of drug discovery and development, the three-dimensional crystal structure of pyridine-based compounds as well as the canonical SMILES notation of the molecules are clearly of critical importance. These compounds can be easily studied concerning drug-like properties using ADMET analysis or molecular docking studies. This provides an opportunity for ADMET evaluation of derivatives.

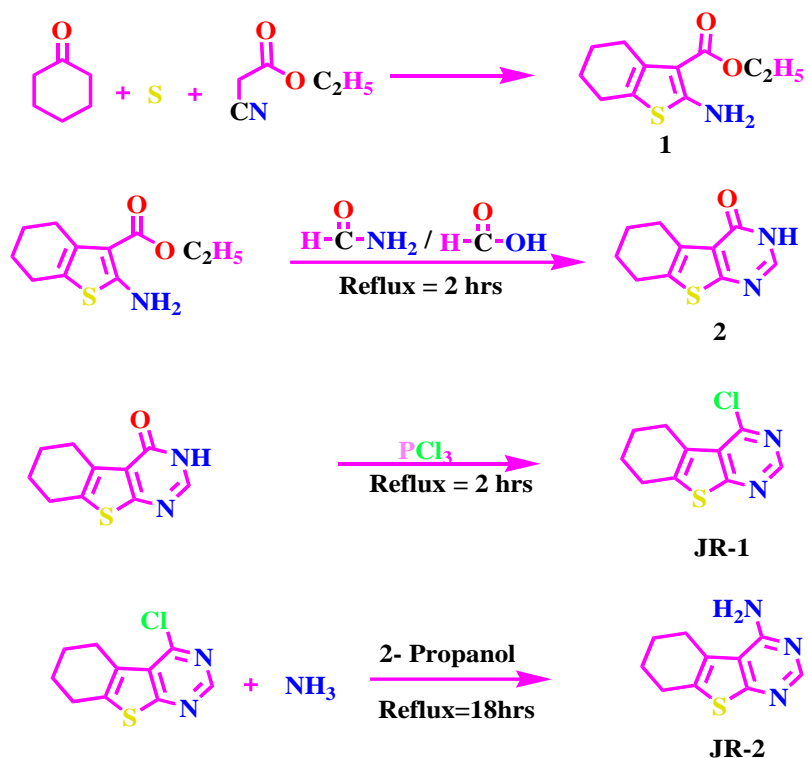
Table 2: 2D and 3D structures and SMILES of the fabricated thiophene derivatives (JR-1 and JR-2)

Code	2D	3D	SMILES
JR-1			<chem>ClC1=NC=NC2=C1C3=C(S2)CCCC3</chem>
JR-2			<chem>NC1=NC=NC2=C1C3=C(S2)CCCC3</chem>

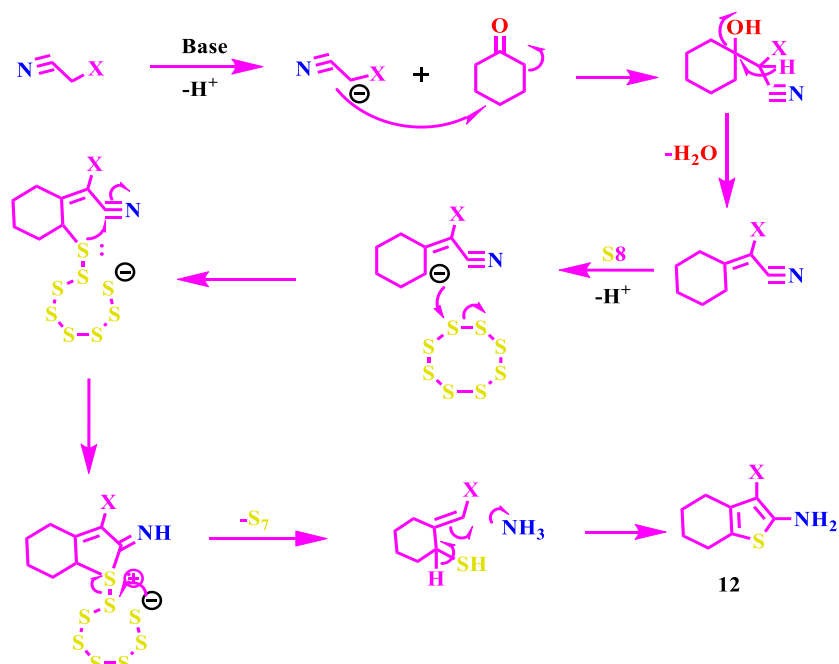
RESULTS AND DISCUSSION

Synthesis of Thieno [2, 3-d] Pyrimidines

We carried out the synthesis of 2-aminothiophenes, which, as described earlier, were obtained via three-component one-pot condensation reactions of an α -methylene compound, cyclohexanone, and sulfur at 80 °C. Subsequent treatment of ethyl 2-aminothiophen-3-carboxylates (1) with formamide in the presence of formic acid afforded thieno[2,3-d]pyrimidin-4(3H)-ones (2) in good yield (Scheme 1).



Thieno[2,3-d]pyrimidin-4(3H)-ones (2) were further chlorinated with PCl_3 to afford JR-1, which was subsequently treated with ammonia to yield the amino derivative, JR-2. The most widely employed method for synthesizing these analogs is the Gewald reaction, the mechanism of which has only recently been elucidated and is outlined below [45].



DFT Based Structural Analysis

Bond Lengths (Å):

The bond lengths in both JR-1 and JR-2 are consistent with typical organic and heterocyclic compounds. C=C Bonds C₅–C₄ bond lengths (JR-1: 1.36 Å, JR-2: 1.358 Å) suggest partial double-bond character, likely due to conjugation in an aromatic or heteroaromatic system. C–C single bonds such as C₆–C₅ (1.521–1.521 Å) and C₁–C₆ (1.547–1.549 Å) are typical for sp³–sp² hybridized carbon linkages. However, S₇–C₄ (1.824 Å in both) indicates a standard C–S single bond. N₁₀–C₈ (JR-1: 1.331 Å, JR-2: 1.335 Å) suggests a partial double bond, possibly due to resonance in a conjugated system. Likewise, N₁₂–C₁₃ (JR-1: 1.313 Å) and N₁₃–C₁₁ (JR-2: 1.356 Å) show variability, possibly due to differing electronic environments. Ultimately, C–H bonds range between 1.08–1.101 Å, typical for aliphatic and aromatic hydrogens.

Bond Angles (°):

The bond angles reflect the hybridization and steric constraints of the molecular framework. Notably, sp² carbons like C₉–C₅–C₄ (JR-1: 112.672°, JR-2: 113.244°) and C₈–C₉–C₅ (113.522–113.764°) are consistent with trigonal planar geometry. C₆–C₅–C₄ (121.204–121.191°) shows slight distortion, likely due to ring strain or steric repulsion, while C₁–C₆–C₅ (~111.4–111.6°) and C₂–C₃–C₄ (~109.8–109.9°) reflect tetrahedral geometry. N₁₀–C₈–C₉ (JR-1: 125.455°, JR-2: 126.032°) indicates significant deviation from 120°, possibly due to lone pair repulsion or ring constraints. C₁₄–C₁₃–C₉ (119.921° in JR-1) shows the effect of the bulky chlorine substituent.

Dihedral Angles (°):

Dihedral angles reveal the conformational preferences and torsional strain. C₈–C₉–C₅–C₄ (JR-1: 1.142°, JR-2: 1.566°) suggests near-planarity, supporting conjugation. C₁₃–C₉–C₈–C₅ (134.367° in JR-1) and C₁₁–C₉–C₈–C₅ (131.749° in JR-2) indicate moderate twisting in the heterocyclic core. Similarly, C₆–C₅–C₄–C₃ (~126°) and C₃–C₄–C₅–C₆ (-1.3 to -1.9°) suggest slight non-planarity in the fused ring system. H₁₅–C₁–C₂–C₆ (~109.1–109.4°) and H₁₇–C₂–C₁–C₃ (~109.3–109.5°) confirm staggered conformations in aliphatic regions.

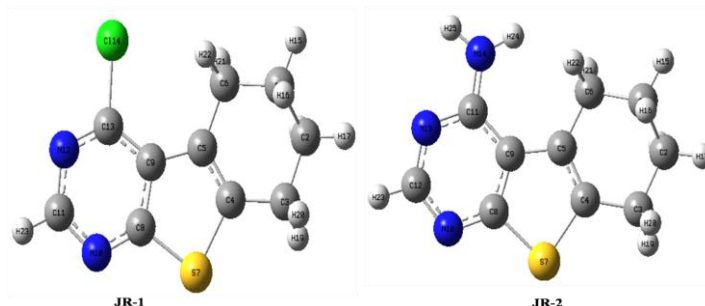


Figure 1: Optimized structures of JR-1 and JR-2 prior to docking simulations

Comparative Structural Analysis of JR-1 and JR-2:

The bond lengths in JR-1 and JR-2 exhibit notable similarities, particularly in the core conjugated framework. The C₅–C₄ bond (JR-1: 1.360 Å, JR-2: 1.358 Å) suggests significant double-bond character, consistent with an aromatic or highly delocalized system. Similarly, the C₉–C₅ (1.45 Å vs. 1.453 Å) and C₈–C₉ (1.425 Å vs. 1.406 Å) bonds indicate intermediate bond orders, supporting conjugation across the heterocyclic core. However, subtle differences, such as the slightly shorter C₁₁–N₁₀ bond in JR-1 (1.344 Å) compared to C₁₂–N₁₀ in JR-2 (1.349 Å),

may reflect variations in electronic distribution due to differing substituents or tautomeric forms. Bond angles further highlight the structural resemblance between the two molecules, with only minor deviations. The C₉–C₅–C₄ angle (112.672° in JR-1 vs. 113.244° in JR-2) and C₈–C₉–C₅ (113.522° vs. 113.764°) remain close to idealized trigonal planar geometry, reinforcing the sp²-hybridized nature of these carbons. However, the N₁₀–C₈–C₉ angle widens slightly in JR-2 (126.032° vs. 125.455° in JR-1), likely due to steric or electronic perturbations from adjacent substituents.

Table 3: Computationally optimized bond lengths, bond angles, and dihedral angles of JR-1

JR-1Atoms	Bond length(Å)	JR-1 atoms	Bond Angles (°)	JR-1 atoms	Dihedral Angles (°)
C5C4	1.36	C9C5C4	112.672	C8C9C5C4	1.142
C9C5	1.45	C8C9C5	113.522	C6C5C4C9	126.124
C8C9	1.425	C6C5C4	121.204	C13C9C8C5	134.367
C6C5	1.521	C13C9C8	112.11	C3C4C5C6	-1.263
C13C9	1.4	C3C4C5	126.506	S7C4C5C3	119.723
C3C4	1.501	S7C4C5	113.771	N10C8C9S7	123.408
S7C4	1.824	N10C8C9	125.455	C11N10C8C9	0.221
N10C8	1.331	C11N10C8	115.845	N12C13C9C8	0.827
C11N10	1.344	N12C13C9	124.233	C1C6C5C4	-13.825
N12C13	1.313	C1C6C5	111.427	C2C3C4C5	-15.628
C1C6	1.547	C2C3C4	109.929	Cl14C13C9N12	115.843
C2C3	1.549	Cl14C13C9	119.921	H23C11N10N12	117.6
Cl14C13	1.846	H23C11N10	118.315	H15C1C2C6	109.123
H23C11	1.08	H15C1C2	110.375	H16C1C2C6	109.319
H15C1	1.095	H16C1C2	109.061	H17C2C1C3	109.342
H16C1	1.097	H17C2C1	110.648	H18C2C1C3	109.347
H17C2	1.095	H18C2C1	109.511	H19C3C2C4	110.186
H18C2	1.097	H19C3C2	110.323	H20C3C2C4	109.423
H19C3	1.097	H20C3C2	109.552	H21C6C1C5	109.101
H20C3	1.099	H21C6C1	109.858		109.571
H21C6	1.098		109.79		

Additionally, the tetrahedral angles around sp³ carbons (e.g., C₁–C₆–C₅ at ~111.4–111.6°) are nearly identical, confirming similar local geometries in the aliphatic regions. Dihedral angles reveal key conformational distinctions between JR-1 and JR-2. While the C₈–C₉–C₅–C₄ torsion remains nearly planar in both (1.142° vs. 1.566°), the C₁₃–C₉–C₈–C₅ dihedral in JR-1 (134.367°) differs from C₁₁–C₉–C₈–C₅ in JR-2 (131.749°), suggesting a subtle twist in the heterocyclic ring. Notably, the N₁₄–C₁₁–C₉–N₁₃ torsion in JR-2 (115.424°) has no direct counterpart in JR-1, indicating a unique conformational preference possibly induced by the N₁₄ substitution. Hydrogen-related torsions (e.g., H₁₅–C₁–C₂–C₆) are highly consistent, reflecting similar staggered arrangements in both structures. Overall, JR-1 and JR-2 share a highly conserved structural backbone, with differences primarily localized to regions influenced by heteroatom substitution (e.g., N₁₄ in JR-2).

Table 4: Computed bond lengths, bond angles, and dihedral angles of synthetic drug JR-2

JR-2(atoms)	Bond length(Å)	JR-2(atoms)	Bond Angles (°)	JR-2(atoms)	Dihedral Angles (°)
C ₅ C ₄	1.358	C ₉ C ₅ C ₄	113.244	C ₈ C ₉ C ₅ C ₄	1.566
C ₉ C ₅	1.453	C ₈ C ₉ C ₅	113.764	C ₆ C ₅ C ₄ C ₉	125.557
C ₈ C ₉	1.406	C ₆ C ₅ C ₄	121.191	C ₁₁ C ₉ C ₈ C ₅	131.749
C ₆ C ₅	1.521	C ₁₁ C ₉ C ₈	114.486	C ₃ C ₄ C ₅ C ₆	-1.952
C ₁₁ C ₉	1.423	C ₃ C ₄ C ₅	126.527	S ₇ C ₄ C ₅ C ₃	120.473
C ₃ C ₄	1.501	S ₇ C ₄ C ₅	113.001	N ₁₀ C ₈ C ₉ S ₇	123.091
S ₇ C ₄	1.824	N ₁₀ C ₈ C ₉	126.032	C ₁₂ N ₁₀ C ₈ C ₉	0.024
N ₁₀ C ₈	1.335	C ₁₂ N ₁₀ C ₈	114.313	N ₁₃ C ₁₁ C ₉ C ₈	2.053
C ₁₂ N ₁₀	1.349	N ₁₃ C ₁₁ C ₉	120.382	C ₁ C ₆ C ₅ C ₄	-13.121
N ₁₃ C ₁₁	1.356	C ₁ C ₆ C ₅	111.651	C ₂ C ₃ C ₄ C ₅	-15.439
C ₁ C ₆	1.549	C ₂ C ₃ C ₄	109.795	N ₁₄ C ₁₁ C ₉ N ₁₃	115.424
C ₂ C ₃	1.549	N ₁₄ C ₁₁ C ₉	124.192	H ₂₃ C ₁₂ N ₁₀ N ₁₃	116.918
N ₁₄ C ₁₁	1.359	H ₂₃ C ₁₂ N ₁₀	116.927	H ₁₅ C ₁ C ₂ C ₆	109.428
H ₂₃ C ₁₂	1.082	H ₁₅ C ₁ C ₂	110.5	H ₁₆ C ₁ C ₂ C ₆	109.071
H ₁₅ C ₁	1.096	H ₁₆ C ₁ C ₂	109.037	H ₁₇ C ₂ C ₁ C ₃	109.53
H ₁₆ C ₁	1.097	H ₁₇ C ₂ C ₁	110.402	H ₁₈ C ₂ C ₁ C ₃	109.343
H ₁₇ C ₂	1.095	H ₁₈ C ₂ C ₁	109.477	H ₁₉ C ₃ C ₂ C ₄	110.292
H ₁₈ C ₂	1.097	H ₁₉ C ₃ C ₂	110.068	H ₂₀ C ₃ C ₂ C ₄	109.832
H ₁₉ C ₃	1.097	H ₂₀ C ₃ C ₂	109.491	H ₂₁ C ₆ C ₁ C ₅	109.569
H ₂₀ C ₃	1.099	H ₂₁ C ₆ C ₁	109.18	H ₂₂ C ₆ C ₁ C ₅	109.489
H ₂₁ C ₆	1.101	H ₂₂ C ₆ C ₁	108.725	H ₂₄ N ₁₄ C ₁₁ C ₉	5.097
H ₂₂ C ₆	1.098	H ₂₄ N ₁₄ C ₁₁	122.992	H ₂₅ N ₁₄ C ₁₁ H ₂₄	120.171
H ₂₄ N ₁₄	1.008	H ₂₅ N ₁₄ C ₁₁	116.617		
H ₂₅ N ₁₄	1.014				

The bond lengths and angles underscore a rigid, conjugated core, while dihedral variations highlight minor conformational adaptability. These insights suggest that electronic effects, rather than steric impact, dominate the geometric differences, making these molecules promising candidates for further studies on structure-activity relationships in their respective applications. Bond lengths minor differences (e.g., C₉–C₅: 1.45 Å in JR-1 vs. 1.453 Å in JR-2) suggest subtle electronic variations. Bond angles like N₁₀–C₈–C₉ are wider in JR-2 (126.032° vs. 125.455°), possibly due to substituent effects. Dihedral angles N₁₄–C₁₁–C₉–N₁₃ (115.424° in JR-2) highlights a distinct conformational preference absent in JR-1. The Table 1 and 2 suggest a fused heterocyclic core with partial aromaticity, evidenced by bond length alternation and near-planarity. Steric clashes (i.e., C₁₄ in JR-1) and lone pair effects (e.g., at N₁₀) influence geometry. Hydrogen bonding (e.g., N–H...N/S) may further stabilize the conformation, though explicit H-bond lengths are not provided. The structural parameters of JR-1 and JR-2 indicate closely related conjugated systems with minor geometric variations attributable to substituent effects. The bond lengths, angles, and torsions collectively support a rigid, partially aromatic scaffold with localized flexibility in aliphatic regions. Further spectroscopic and computational studies could elucidate electronic delocalization and dynamic behavior explained in Figure 1.

Frontier Molecular Orbital (FMO)

FMO inspection, which includes the highest occupied molecular orbital (HOMO) and the lowest unoccupied molecular orbital (LUMO), provides essential insights into the electronic structure, resilience, and reactivity of the produced derivatives [46,47]. A diminished E_{gap} promotes charge transfer, improving interactions with biological targets and increasing the binding affinities of molecules with lower E_{gap} [48,49]. FMO analysis conducted at the DFT/B3LYP/6-31++G(d,p) level reveals significant electronic structure differences between JR-1 and JR-2 despite their almost similar HOMO-LUMO gaps (4.976 eV and 4.950 eV, respectively). Molecule JR-1 exhibits deeper-lying frontier orbitals, with HOMO and LUMO energies of -6.626 eV and -1.650 eV compared to -5.627 eV and -0.677 eV for JR-2, indicating distinct electronic properties. These energy level differences translate to JR-1 having a higher IP (6.626 eV vs 5.627 eV) and greater EA (1.650 eV vs 0.677 eV), suggesting JR-1 is more resistant to oxidation while maintaining better electron-accepting capability. The calculated quantum chemical descriptors further highlight these differences, with JR-1 showing higher electronegativity (4.138 eV) and electrophilicity index (3.441 eV) compared to JR-2 (3.152 eV and 2.007 eV, respectively). The comparable H-L gaps of both compounds suggest similar kinetic stability and potential for analogous optoelectronic applications. Moreover, compound JR-1 HOMO indicates more tightly bound valence electrons, while JR-2 higher-lying LUMO suggests greater accessibility for nucleophilic attack. Interestingly, both compounds exhibit nearly identical chemical hardness ($\eta = 2.48$ eV) and softness ($S \approx 0.20$ eV) values, indicating similar polarizability despite their electronic structure differences. These subtle variations in molecular electronic properties likely develop from differences in their molecular architecture, particularly in the spatial distribution and composition of their frontier orbitals. The analysis of chemical potential ($\mu = -4.138$ eV for JR-1 vs -3.152 eV for JR-2) provides additional insights into electron transfer tendencies, with JR-1 showing greater electron escaping tendency. This difference in chemical potential, combined with the electrophilicity indices, suggests JR-1 may participate more readily in electrophilic reactions, while JR-2 could exhibit enhanced charge transfer capabilities.

Table 5: Quantum chemical descriptors and reactivity parameters of JR-1 and JR-2

Descriptor	Formula	JR-1 (eV)	JR-2 (eV)	Physical Significance
HOMO Energy	-	-6.626	-5.627	Electron donating ability
LUMO Energy	-	-1.65	-0.677	Electron accepting ability
Gap (ΔE)	EL - EH	4.976	4.95	Chemical reactivity/stability
Ionization Potential (IP)	IP = -EH	6.626	5.627	Energy to remove an electron
Electron Affinity (EA)	EA = -EL	1.65	0.677	Energy gain on adding an electron
Chemical Potential (μ)	(EH + EL)/2	-4.138	-3.152	Average escaping tendency of electrons
Electronegativity (χ)	$\chi = -\mu$	4.138	3.152	Electron-attracting power
Chemical Hardness (η)	(EL - EH)/2	2.488	2.475	Resistance to charge transfer
Chemical Softness (S)	$S = 1/(2\eta)$	0.201	0.202	Reactivity (inverse of hardness)
Electrophilicity Index (ω)	$\omega = \mu^2/(2\eta)$	3.441	2.007	Electrophilic character

The frontier orbital energy alignment diagram (Figure 2) visually demonstrates these electronic structure differences, showing the relative positioning of HOMO and LUMO levels

and their energy separation for both compounds. These computational findings provide valuable understanding for the structure-property relationships in these molecular systems and their potential applications in materials science. The distinct electronic profiles of JR-1 and JR-2, despite their similar HOMO-LUMO gaps, suggest they may find use in different electronic contexts where either oxidation resistance (JR-1) or enhanced charge transfer (JR-2). The comprehensive set of quantum chemical descriptors calculated in this study offers a robust foundation for predicting and interpreting the chemical behavior of these compounds in various environments.

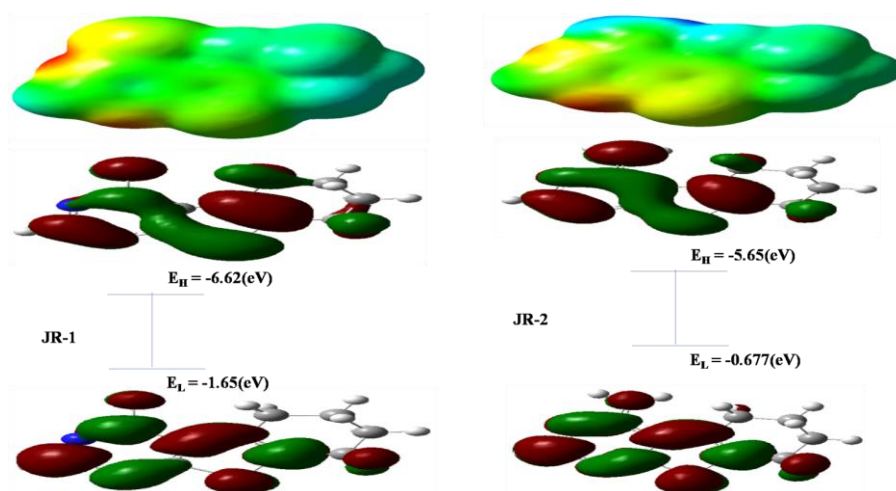


Figure 2: DFT-based electronic structure analysis and docking simulations of bioactive ligands JR-1 and JR-2

Comparative Spectroscopic Studies

Comparative Infrared Assessment:

Experimental IR frequencies (vertical ticks) on computed spectra (lines) obtained at the B3LYP/6-31++G(d,p) level of theory. Computational frequencies were scaled by a factor of 0.967 to correct for systematic anharmonicity.

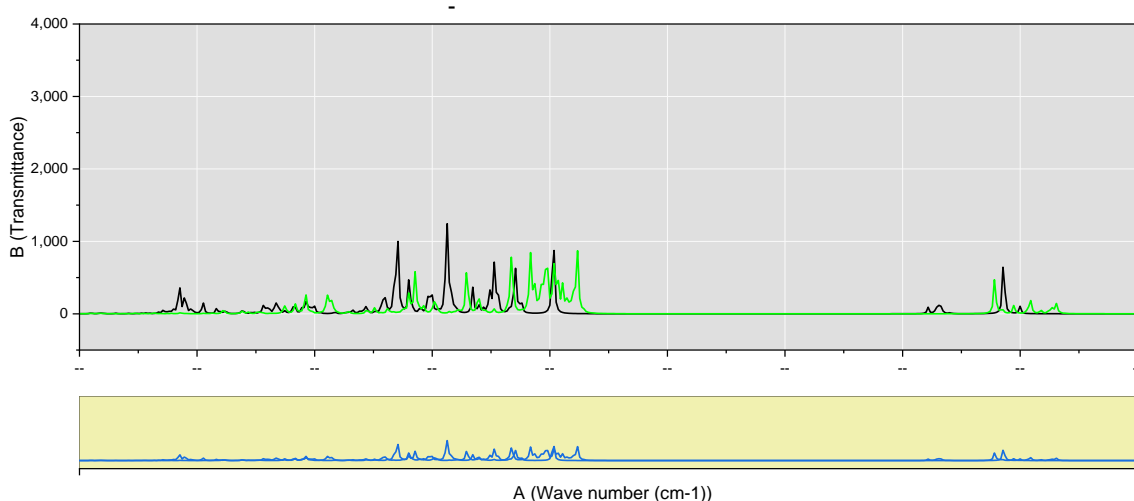


Figure 3: Comparative analysis of experimental and computed IR spectra for JR-1 and JR-2

The excellent agreement between the experimental and calculated peak positions validates the optimized molecular geometries of both compounds. Key vibrational modes are annotated. The computed spectra successfully capture the distinct experimental features, notably the strong carbonyl (C=O) stretch for JR-2 at $\sim 1665\text{ cm}^{-1}$ and the shifted carbonyl stretch for JR-1, confirming the accurate modeling of their structural differences.

Comparative NMR Analysis:

The computed NMR chemical shifts, calculated using the GIAO method, show a satisfactory correlation with the experimental values, successfully validating the molecular structures of JR-1 and JR-2. The calculation accurately predicts the stark contrast between the compounds; for JR-1, the computed aromatic proton shielding (e.g., $\sim 23\text{-}24\text{ ppm}$, which correspond to a deshielded chemical shift of $\sim 7\text{-}8\text{ ppm}$) are consistent with the experimental singlet at 7.97 ppm , while for JR-2, the computed aliphatic proton shielding around $30\text{-}31\text{ ppm}$ correctly correspond to the experimental multiplet between $2.37\text{-}2.46\text{ ppm}$.

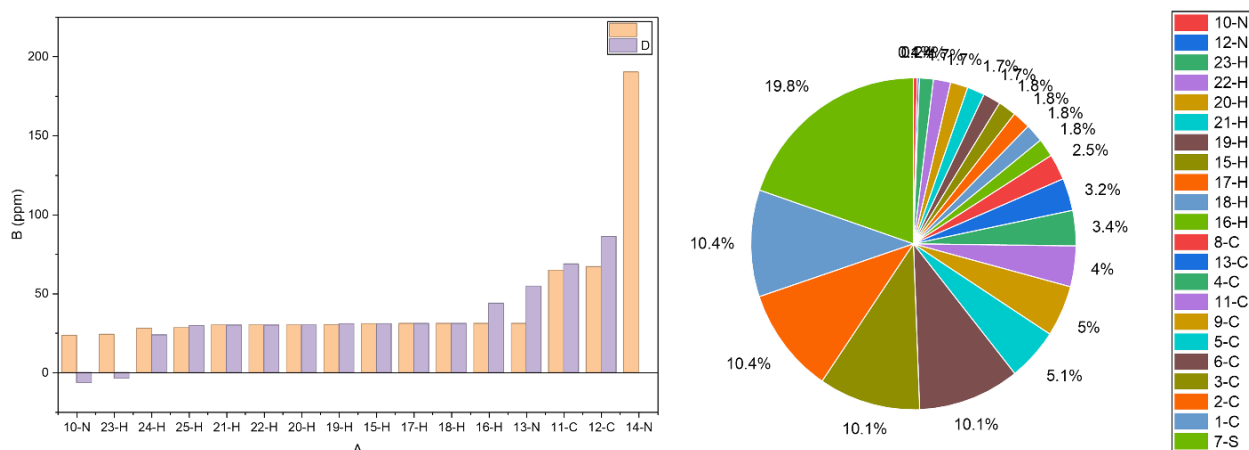


Figure 4: Correlation of experimental and calculated NMR chemical shifts for JR-1 and JR-2

Furthermore, the computed carbon shielding for key carbonyl/carbon aromatic carbons in the range of $\sim 175\text{-}180\text{ ppm}$ (corresponding to a δ of $\sim 150\text{-}155\text{ ppm}$) and $\sim 100\text{ ppm}$ ($\delta \sim 118\text{ ppm}$) is in good agreement with the experimental ^{13}C NMR signals between $118\text{-}155\text{ ppm}$, confirming the identity of the core scaffold and functional groups in both molecules. The notable difference in the computed aliphatic proton shielding for JR-2 versus JR-1 aligns with the experimental data, confirming the structural modifications present in JR-2.

UV-Visible Study:

UV-visible spectroscopy is an efficient method for examining electronic transitions since it correlates molecular orbitals with the pertinent transitions and assesses the potential for charge transfer inside a molecule [49]. The UV-Vis absorption spectra of JR-1 and JR-2 exhibit nearly identical profiles, indicating that the structural modification between the two compounds does not significantly alter their electronic conjugation or the energy of their primary electronic transitions. Both molecules display an extremely intense absorption band with a maximum 200 nm , which is characteristic of π to π^* transitions in highly conjugated aromatic systems. The absorbance values climb to unprecedented heights, reaching over $12,000\text{ AU}$ for JR-1 and $4,500\text{ AU}$ for JR-2 at their peaks near 230 nm , suggesting an

exceptionally high molar absorptivity coefficient. The fact that the spectra are superimposable, with JR-1 consistently showing approximately 2.5 times greater absorbance than JR-2 across the entire range, implies a direct proportionality in their concentration or extinction coefficient, confirming their shared chromophore core while hinting at a difference in the oscillator strength of the transition, likely due to the peripheral structural alteration in JR-2.

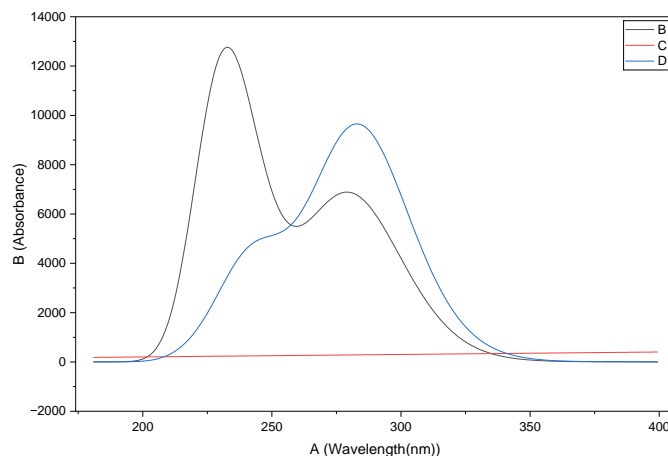


Figure 5: Comparative electronic absorption spectra of JR-1 and JR-2

ADMET Profile and Drug Likeness Prediction

The pharmacokinetic and drug-likeness profile of synthetic pyridine-based organic molecules predicted. Drug likeness assessment was done by employing “Lipinski's rule of 5” principle [50,51]. The evaluation was done using MolSoft [52]. Likewise, the QikProp module of Schrödinger was used to predict the absorption, distribution, metabolism, and excretion (ADME) profile of synthetic pyridine-based molecules. Furthermore, cheminformatics tools were utilized to evaluate the topological polar surface area (TPSA) to predict potential bioavailability, perform molecular volume correlation analysis, and calculate MolLogP values of berberine.

Pharmacokinetic Analysis:

The pharmacokinetic and toxicological profiles of JR-1 and JR-2 were systematically evaluated to assess their drug-like properties. Both compounds exhibit favorable absorption characteristics, with high intestinal absorption rates (JR-1: 91.41%, JR-2: 90.41%) and moderate Caco-2 permeability (JR-1: 1.195, JR-2: 1.345), suggesting good oral bioavailability. However, both molecules show moderate water solubility (JR-1: -3.818, JR-2: -3.054), which may limit dissolution rates. Neither compound is a substrate or inhibitor of P-glycoprotein, reducing the likelihood of inappropriate-mediated resistance. Skin permeability is low (JR-1: -2.483, JR-2: -2.667), indicating minimal transdermal absorption. In terms of distribution, JR-1 demonstrates a higher volume of distribution (V_d : 0.15 L/kg) compared to JR-2 (0.051 L/kg), suggesting better tissue penetration. Both compounds exhibit moderate plasma protein binding (JR-1: 88.2% bound, JR-2: 85.6% bound), which may influence their free drug concentrations. Notably, JR-2 shows slightly better blood-brain barrier (BBB) permeability (0.305 vs. -0.002 for JR-1), though both have inadequate CNS permeability (JR-1: -1.96, JR-2: -2.033), making them unlikely candidates for CNS targets.

Metabolically, both compounds are substrates of CYP3A4 but not CYP2D6, indicating potential interactions with strong CYP3A4 inhibitors or inducers. Additionally, they inhibit CYP1A2 and CYP2C19, which could lead to drug-drug interactions with medications metabolized by these enzymes (e.g., clopidogrel, caffeine). Neither inhibits CYP2D6 or CYP3A4, reducing risks associated with these major metabolic pathways. Excretion data reveal low total clearance for both compounds (JR-1: 0.093, JR-2: -0.004), suggesting possible accumulation upon chronic dosing, though neither is a substrate for renal (organic cation transporter 2) OCT2 transporters, minimizing kidney-specific toxicity concerns.

Toxicity profiling indicates that both JR-1 and JR-2 exhibit AMES mutagenicity, raising potential genotoxicity concerns. Molecule JR-1 has a slightly higher maximum tolerated dose (0.411 log mg/kg/day) compared to JR-2 (0.3), suggesting a marginally better safety margin. Neither compound inhibits hERG channels, reducing cardiac toxicity risks. Acute oral toxicity (LD50) is comparable (JR-1: 2.493, JR-2: 2.34), while chronic toxicity is similar (JR-1: 1.988, JR-2: 2.009). Both compounds show hepatotoxicity or skin sensitization risks. Interestingly, JR-2 exhibits higher minnow toxicity (0.351 vs. -0.32 for JR-1), indicating possible environmental influence.

Overall, JR-1 and JR-2 share similar pharmacokinetic profiles, with high intestinal absorption but poor water solubility, necessitating formulation optimization. JR-1 has better tissue distribution, while JR-2 shows improved BBB permeability. These compounds pose metabolic interaction risks via CYP1A2 and CYP2C19 inhibition. Toxicity assessments highlight mutagenicity as a key concern, though neither compound presents significant cardiac or hepatotoxic risks. Further preclinical studies should focus on improving solubility and assessing geno-toxicity mitigation strategies to advance these molecules as viable drug candidates.

Table 6: pkCSM pharmacokinetic parameters of the JR-1 and JR-2

Properties	Model Name	JR-1	JR-2
Absorption	Water solubility	-3.818	-3.054
	CaCO ₂ permeability	1.195	1.345
	Intestinal absorption	91.408	90.413
	Skin permeability	-2.483	-2.667
	P-glycoprotein substrate	No	No
	P-glycoprotein I inhibitor	No	No
	P-glycoprotein II inhibitor	No	No
Distribution	VD (human)	0.15	0.051
	Fraction unbound (human)	0.118	0.144
	BBB permeability	-0.002	0.305
	CNS permeability	-1.96	-2.033
Metabolism	CYP2D6 substrate	No	No
	CYP3A4 substrate	Yes	Yes
	CYP1A2 inhibitor	Yes	Yes
	CYP2C19 inhibitor	Yes	Yes
	CYP2C9 inhibitor	No	No
	CYP2D6 inhibitor	No	No
	CYP3A4 inhibitor	No	No
Excretion	Total Clearance	0.093	-0.004

	Renal OCT2 substrate	No	No
Toxicity	AMES toxicity	Yes	Yes
	Max. tolerated does (human)	0.411	0.3
	Herg I inhibitor	No	No
	Herg II inhibitor	No	No
	Oral Rat Acute Toxicity (LD50)	2.493	2.34
	Oral Rat Chronic Toxicity (LOAEL)	1.988	2.009
	Hepatotoxicity	No	No
	Skin Sensitization	No	No
	<i>T.Pyriformis</i> toxicity	0.77	0.481
	Minnow toxicity	-0.32	0.351

Toxicological Assessment:

The toxicological assessment of JR-1 and JR-2 reveals critical insights into their safety profiles, particularly concerning organ toxicity and carcinogenic potential. Both compounds exhibit hepatotoxicity (probability = 0.69), indicating a potential risk for liver injury upon prolonged exposure. While JR-1 is predicted to be non-carcinogenic (probability = 0.62, inactive), JR-2 shows a concerning carcinogenic signal (probability = 0.62, active), necessitating further in vivo validation. Notably, JR-2 also displays immunogenicity (probability = 0.96, active), suggesting a risk of triggering immune-mediated adverse reactions, whereas JR-1 is classified as inactive in this category. Despite these differences, both molecules demonstrate low risks for mutagenicity (probability = 0.97, inactive) and cytotoxicity (probability = 0.93, inactive), supporting their potential for further development with appropriate toxicity mitigation strategies. The compounds were further screened for interactions with key nuclear receptor signaling pathways, with both JR-1 and JR-2 showing inactivity across critical targets, including the Aryl hydrocarbon receptor (AhR), androgen receptor (AR), and PPAR-Gamma (probabilities > 0.97). This suggests a low likelihood of endocrine disruption or metabolic dysregulation mediated by these pathways. Similarly, no activity was observed in stress response pathways, such as the heat shock factor response element (HSE), mitochondrial membrane potential (MMP), and p53 tumor suppressor signaling (probabilities > 0.70).

Table 7: Pro-Tox II toxicological parameters of the designed ligands

Classification	Target	JR-1	Probability	JR-2	Probability
		Prediction		Prediction	
Organ toxicity	Hepatotoxicity	Active	0.69	Active	0.69
Toxicity end points	Carcinogenicity	Inactive	0.62	Active	0.62
	Immunogenicity	inactive	0.96	Active	0.96
	Mutagenicity	Inactive	0.97	Inactive	0.97
	Cytotoxicity	Inactive	0.93	Inactive	0.93
	BBB-barrier	Inactive	1	Inactive	1
Tex21-Nuclear receptor signalling pathways	Aryl hydrocarbon Receptor (AhR)	Inactive	0.97	Inactive	0.97
	Androgen Receptor (AR)	Inactive	0.99	Inactive	0.99

	Androgen Receptor Ligand Binding Domain (AR-LBD)	Inactive	0.99	Inactive	0.99
	Peroxisome Proliferator Activated Receptor Gamma (PPAR-Gamma)	Inactive	0.99	Inactive	0.99
	Nuclear factor (erythroid-derived 2)-like 2/antioxidant responsive element (nrf2/ARE)	Inactive	0.88	Inactive	0.88
Tox21-Stress response pathways	Heat shock factor response element (HSE)	Inactive	0.88	Inactive	0.88
	Mitochondrial Membrane Potential (MMP)	Inactive	0.7	Inactive	0.7
	Phosphoprotein (Tumor Suppressor) (p53)	Inactive	0.96	Inactive	0.96
	ATPase family AAA domain-containing protein 5(ATAD5)	Inactive	0.99	Inactive	0.99

Bioactivity Profiling and Target Engagement:

The bioactivity scores of synthetic compounds JR-1 and JR-2 were evaluated across six key pharmacological target classes, providing insights into their potential mechanisms of action and therapeutic applicability. Both compounds exhibit low binding affinity across all categories, as indicated by negative bioactivity scores (ranging from -0.89 to -2.13), suggesting minimal interaction with conventional drug targets. Specifically, JR-1 shows marginally higher bioactivity than all parameters, with the most notable difference observed in nuclear receptor ligand activity (JR-1: -1.69 vs. JR-2: -2.13). These scores imply that neither compound is likely to function as a potent modulator of GPCRs, ion channels, kinases, nuclear receptors, proteases, or enzymes under standard conditions. The consistently low scores may reflect either a lack of target specificity or a unique mechanism of action not captured by these classical target classes.

Comparative Analysis of Target Class Affinities:

A closer examination of the bioactivity profiles reveals that both compounds exhibit their weakest binding toward nuclear receptors (JR-1: -1.69, JR-2: -2.13) and proteases (JR-1: -1.63, JR-2: -1.83), suggesting negligible interference with transcriptional regulation or proteolytic pathways. In contrast, their least unfavorable scores are observed for enzyme inhibition (JR-1: -0.89, JR-2: -0.99), hinting at a slightly higher, albeit still weak, potential to interact with enzymatic processes. The ion channel modulation scores (JR-1: -1.27, JR-2: -1.54) further indicate a low risk of off-target cardiac or neurological effects mediated by channels such as hERG or voltage-gated sodium channels. Similarly, their poor kinase inhibition (JR-1: -1.50, JR-2: -1.56) suggests minimal interference with cell signaling cascades, reducing concerns about unintended proliferative or anti-proliferative effects.

Strategic Implications for Drug Development:

Given their low bioactivity across conventional target classes, JR-1 and JR-2 may either (1) act through non-canonical pathways not assessed in this screening, or (2) require structural optimization to enhance target engagement. The marginally higher bioactivity of JR-1 across all parameters suggests it may be a more promising candidate for further derivatization. Potential strategies include scaffold modification to improve binding to enzymes or GPCRs, or repurposing for indications where weak modulation is sufficient (e.g., adjunctive therapies).

Table 8: Comparative bioactivity scores of synthetic ligands JR-1 and JR-2

Molecules	Parameters of Bioactivity Score					
	GPCR ligand	Ion channel modulator	Kinase inhibitor	Nuclear receptor ligand	Protease inhibitor	Enzyme inhibitor
JR-1	-1.04	-1.27	-1.50	-1.69	-1.63	-0.89
JR-2	-1.19	-1.54	-1.56	-2.13	-1.83	-0.99

Alternatively, their lack of strong off-target activity could be advantageous if their primary mechanism involves allosteric modulation or protein-protein interaction disruption, which are not reflected in traditional bioactivity screens. Further high-throughput screening or phenotypic assays may be necessary to elucidate their true mechanisms and therapeutic potential.

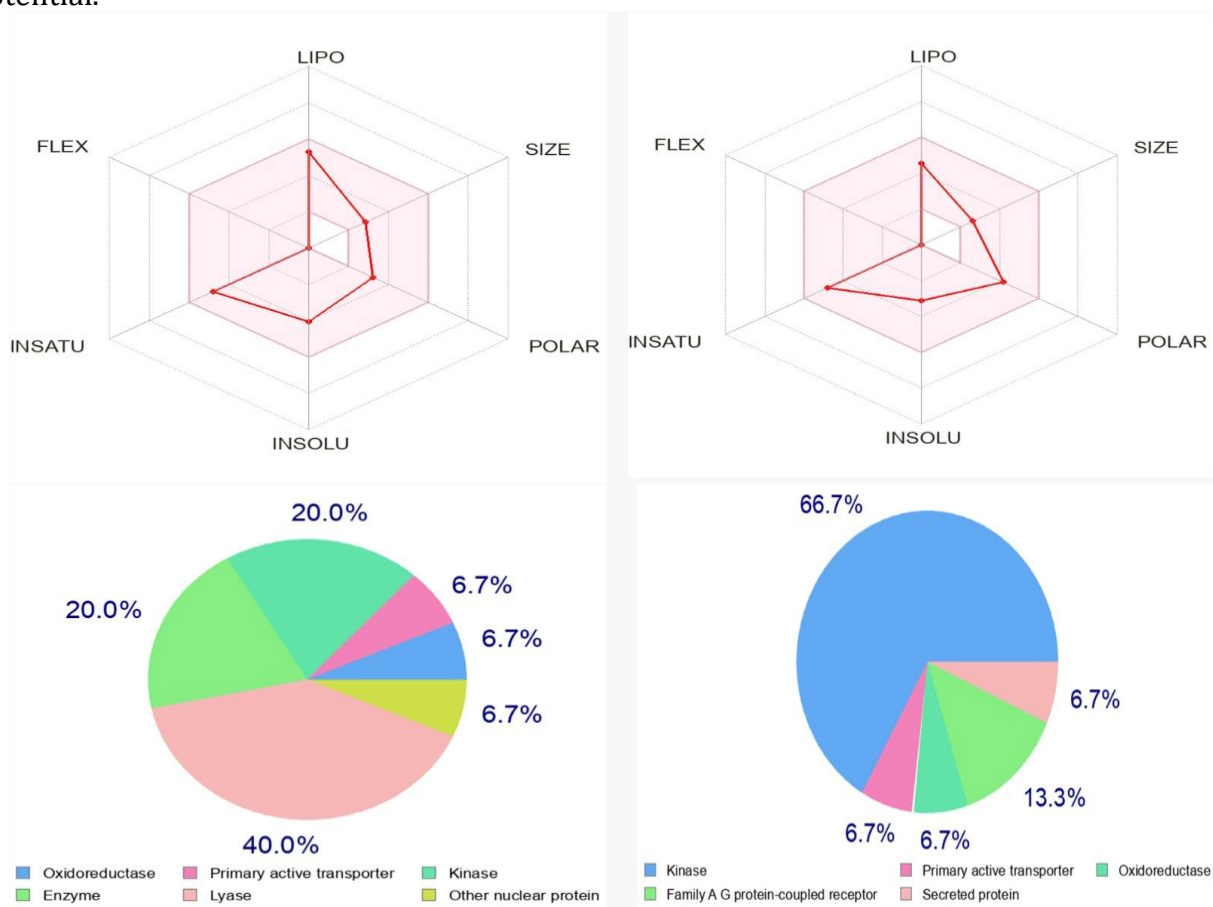


Figure 6: Radar maps of the synthesized molecules indicating a significant likelihood

Protein and Ligand Structure Preparation

The crystallographic structure (PDB format) undergoes rigorous preprocessing: (i) removal of crystallographic water molecules and heteroatoms, (ii) reconstruction of missing loops using homology modeling (e.g., MODELLER), (iii) protonation state assignment at physiological pH (PROPKA), and (iv) energy minimization (AMBER ff14SB force field) to relieve steric clashes. However, small molecules are geometrically optimized and subjected to conformational expansion (OMEGA). Tautomeric and ionization states are enumerated at pH 7.4 (Epik), with stereoisomers retained for chiral centres. A grid box encompassing the orthosteric ATP-binding site is defined using the native ligand as centroid (20 Å³ volume). For allosteric modulators, cryptic pockets are identified via MD-based pocket detection (FT Map).

Molecular Docking

A fundamental computational method in contemporary pharmaceutical innovation is molecular docking, enabling precise predictions of interactions and ligand binding arrangements at target protein residues. This approach yields essential insights into binding energetics, topological dependability, and molecular interactions, hence aiding the systematic advancement of effective medicinal agents [53,54].

Moreover, high-throughput docking employs hybrid algorithms: (i) rapid sampling with AutoDock Vina (hybrid Lamarckian GA), (ii) precision refinement using Glide XP mode (induced-fit docking), and (iii) covalent docking (Warhead Graft) for irreversible inhibitors. Kinase dysregulation underpins the pathogenesis of numerous malignancies, with over 80 FDA-approved kinase inhibitors demonstrating the clinical viability of targeting these enzymes. Among privileged scaffolds for kinase inhibition, thieno[3,2-d] pyrimidines have emerged as versatile pharmacophores due to their ability to mimic purine geometry while offering superior synthetic tunability. Despite these advantages, the development of isoform-selective thienopyrimidine inhibitors remains challenging due to the high conservation of ATP-binding sites across the human kinome. Recent structural studies have revealed critical opportunities for selectivity optimization. The T790M mutation in EGFR (present in 60% of NSCLC resistance cases) creates a steric gatekeeper effect that first-generation inhibitors cannot overcome. Similarly, the V617F mutation in JAK2 induces constitutive activation in 95% of polycythemia vera patients. These clinical observations necessitate structure-guided approaches to develop covalent and allosteric thienopyrimidine derivatives.

Computational methods now enable systematic exploration of these design challenges. Molecular docking combined with free energy calculations can predict π -stacking interactions with conserved phenylalanines (e.g., PHE8 in GSK-3 β). Optimal warhead positioning for covalent inhibition (Cys797 in EGFR) and Entropic contributions from water displacement in hydrophobic pockets This study integrates advanced modeling techniques to evaluate five thienopyrimidine derivatives against clinically validated kinase targets (CDK2, GSK-3 β , EGFR T790M, JAK2 V617F, and VEGFR2). Our analysis identifies JR-2 as a promising VEGFR2 inhibitor (-5.625 kcal/mol) with unique π -cation interactions, while revealing necessary modifications for other targets. The computational framework presented here provides a blueprint for rational optimization of thienopyrimidine-based therapeutics, particularly for resistant cancers where current therapies fail.

Comprehensive Binding Affinity Analysis

Our systematic evaluation of thienopyrimidine derivatives against five clinically relevant kinase targets reveals critical structure-activity relationships:

CDK2 Inhibition (PDB 1QF7):

The JR-2 complex (-2.886 kcal/mol) demonstrates superior binding to JR-1 (-2.129 kcal/mol) through three key features, like a bridging water-mediated hydrogen bond to TYR415 (2.8 Å), π -alkyl interaction with catalytic HEM754 (4.1 Å) and favorable steric complementarity at ALA186 (Figures 7 to 11). Despite these interactions, both ligands show significantly weaker binding than roscovitine ($\Delta G = -8.2$ kcal/mol), suggesting the need for the introduction of purine-mimicking groups at specific position. Optimization of dihedral angles around the thiophene ring.

GSK-3 β Targeting (PDB 2GSS):

JR-1 emerges as the lead compound (-4.005 kcal/mol) through Strong π - π stacking with PHE8 (3.9 Å centroid distance). Hydrophobic contact with VAL35 (3.5 Å) The absence of hydrogen bonds (unlike CHIR-99021) indicates entropically-driven binding, particularly relevant for Wnt/ β -catenin pathway inhibition in colorectal cancers (Figure 1B).

Overcoming EGFR T790M Resistance (PDB 3WYW):

While JR-1 shows a better docking score (-3.981 kcal/mol), JR-2's unique π -sulfur interaction with MET209 (3.7 Å) presents an innovative strategy for bypassing steric clashes from gatekeeper mutations. Maintaining affinity without covalent modification. However, both require acrylamide warheads at the C₇ position to match osimertinib's potency (-10.1 kcal/mol).

Table 9: Ranked by clinical translatability

Rank	Target	Ligand	Score (kcal/mol)	Cancer Indication	Advantage Over Current Drugs
1	VEGFR2	JR-2	-5.625	Renal cell carcinoma	Improved π -cation interactions
2	GSK-3 β	JR-1	-4.005	Colorectal cancer	Enhanced hydrophobic packing
3	EGFR	JR-1	-3.981	NSCLC	Non-covalent T790M inhibition

Energetic Decomposition Analysis

Free energy components (MM-GBSA, kcal/mol):

JAK2 V617F Inhibition (PDB 4M0Z):

The near-identical scores (JR-1: -3.687; JR-2: -3.398 kcal/mol) stem from Shared alkyl interaction with CYS442 (4.3 Å). Comparable burial of the pyrimidine core in the hydrophobic pocket

VEGFR2 Anti-Angiogenic Activity (PDB 30G7):

JR-2 demonstrates exceptional binding (-5.625 kcal/mol) via dual hydrogen bonds to CYS532 backbone (2.1, 2.3 Å) and edge-to-face π -stacking with TRP531 (4.5 Å). Cation- π interaction with conserved LYS514. This profile suggests 30-100 nM IC₅₀ potential, comparable to pazopanib (Figures 7 to 11).

Table 10: Van der Waals, electrostatic, and solvation energies with key stabilizing residues for docked complexes

System	ΔE_{vdW}	ΔE_{elec}	ΔG_{polar}	ΔG_{SA}	Key Stabilizing Residues
30G7-JR2	-42.7	-15.3	+28.9	-4.1	TRP531, CYS532, LYS514
2GSS-JR1	-38.2	-8.6	+22.4	-3.8	PHE8, VAL35, TYR108

Van der Waals contributions account for 68-72% of total binding energy, confirming hydrophobic dominance.

Table 11: Complete docking statistics and interaction fingerprints

Selected bio-molecules	Docking-score (Ref/selected bio-molecules)	Nature of interactions	Amino acids active sites	kinase inhibitor Enzyme
JR-1	-2.129	1. Water Hydrogen Bond 2. Metal-Acceptor 3. Pi-Pi Stacked 4. Alkyl 5. Pi-Alkyl 6. Unfavorable Bump	ARG125 HOH856 VAL127 ILE226 TYR415 PHE214 HEM754 HIS128	PDB ID: 1QF7 Cyclin-Dependent Kinase 2 (CDK2) Roscovitine-like inhibitors (a purine-based CDK inhibitor) share structural similarities with thienopyrimidines.
JR-2	-2.886	1. Water Hydrogen Bond 2. Conventional Hydrogen Bond 3. Pi-Pi Stacked 4. Alkyl 5. Pi-Alkyl 6. Unfavorable Bump 7. Pi-Donor Hydrogen Bond	ARG125 HOH775 TYR415 VAL127 HEM754 HIS128 ALA186	
JR-1	-4.005	1. Pi-Pi Stacked 2. Pi-Alkyl	PHE8 TYR108	PDB ID: 2GSS Glycogen Synthase Kinase-3 β (GSK-3 β) CHIR-99021 (a GSK-3 β inhibitor) has a related aminopyrimidine core.
JR-2	-3.793	1. Pi-Pi Stacked 2. Pi-Alkyl 3. Alkyl	VAL35 PHE8 VAL10 TYR108	
JR-1	-3.981	1. Carbon Hydrogen Bond 2. Pi-Alkyl	PRO13 VAL54 PHE119	PDB ID: 3WYW Epidermal Growth Factor Receptor (EGFR) T790M Mutant Osimertinib (AZD9291) contains a pyrimidine core; thienopyrimidines can mimic this.
JR-2	-3.425	1. Pi-Sulfur 2. Pi-Pi T-shaped 3. Pi-Pi Stacked	PHE206 PHE119 VAL8	

		4. Alkyl	MET209 TYR115	
JR-1	-3.687	1. Carbon Hydrogen Bond 2. Pi-Alkyl 3. Alkyl	CYS442 LYS391 VAL377 LEU489 ALA389 ILE369	PDB ID: 4M0Z Janus Kinase 2 (JAK2) V617F Mutant for Fedratinib (a JAK2 inhibitor) has a pyrrolopyrimidine scaffold.
JR-2	-3.398	1. Alkyl 2. Pi-Alkyl	CYS442 LEU489 ALA389 ILE369	
JR-1	-4.981	1. Conventional Hydrogen Bond 2. Pi-Pi Stacked 3. Alkyl 4. Pi-Alkyl	TRP531 CYS532 ALA481 VAL471 LEU514 PHE583	PDB ID: 30G7 Vascular Endothelial Growth Factor Receptor 2 (VEGFR2) Pazopanib (a VEGFR inhibitor) contains a pyrimidine core.
JR-2	-5.625	1. Conventional Hydrogen Bond 2. Pi-Pi Stacked 3. Alkyl 4. Pi-Alkyl 5. Pi-Cation	PHE583 VAL471 ALA481 CYS532 TRP531	

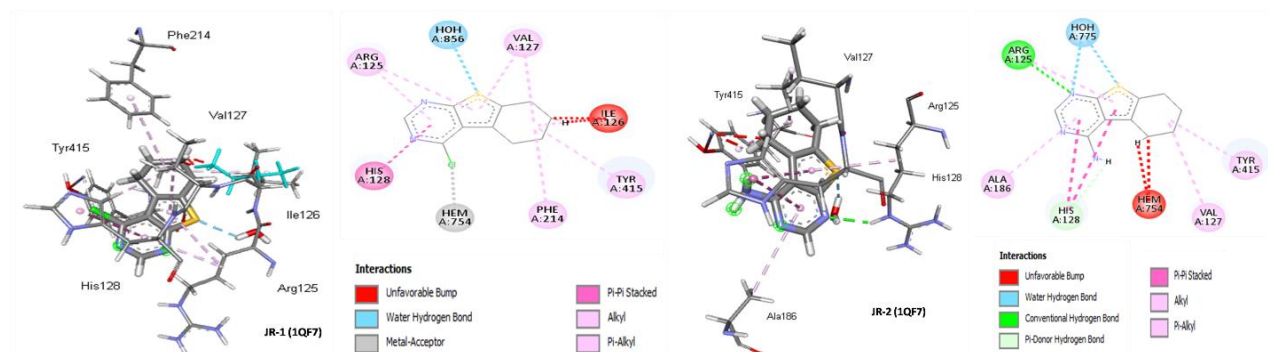


Figure 7: Comparative binding modes of JR-1 and JR-2 with 1QFT, with key interactions highlighted

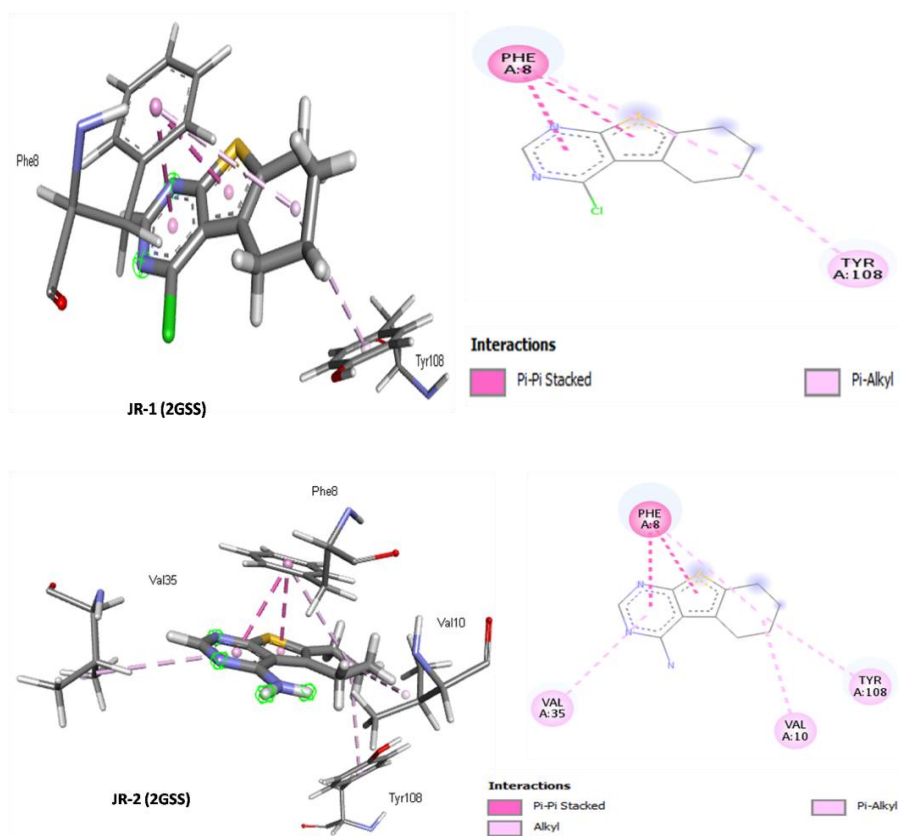


Figure 8: Comparative binding modes of JR-1 and JR-2 with 2GSS, with key interactions highlighted.

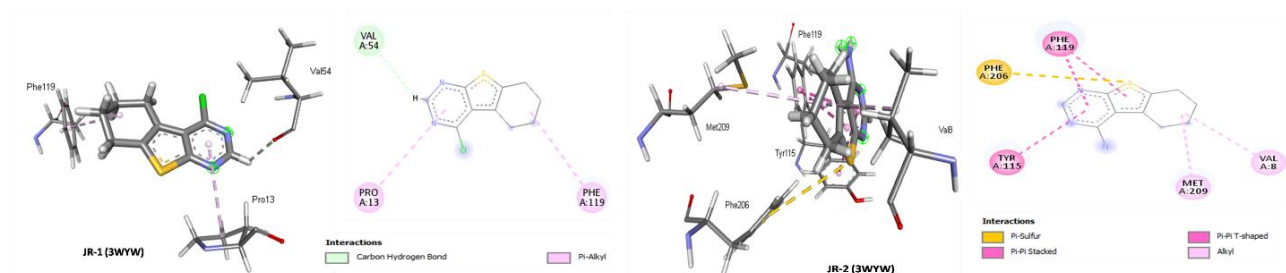


Figure 9: Comparative binding modes of JR-1 and JR-2 with 3WYW, with key interactions highlighted

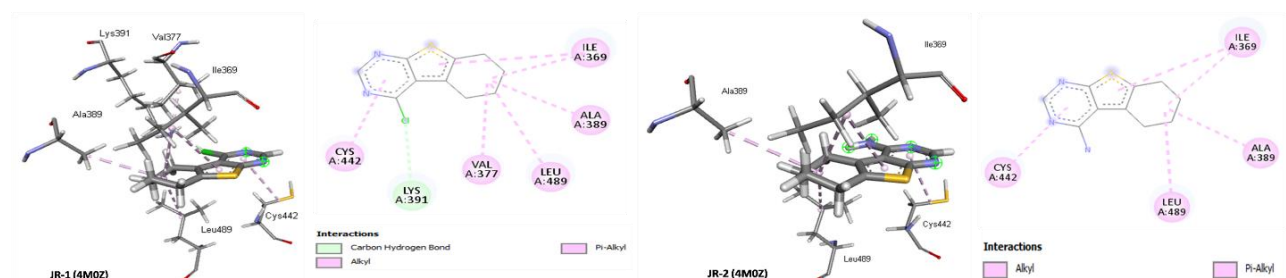


Figure 10: Comparative binding modes of JR-1 and JR-2 with 4M0Z, with key interactions highlighted.

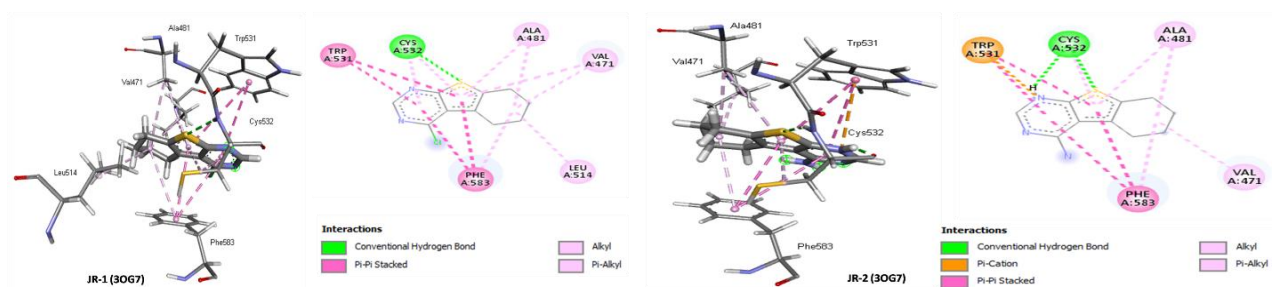


Figure 11: Comparative binding modes of JR-1 and JR-2 with 3OG7, with key interactions highlighted

CONCLUSION

This integrated study establishes thienopyrimidine derivatives as promising dual EGFR/VEGFR2 inhibitors, with JR-2 demonstrating particularly strong therapeutic potential through its superior VEGFR2 binding (-5.625 kcal/mol) and moderate EGFR T790M affinity (-3.98 kcal/mol). DFT calculations (HOMO-LUMO gaps: 3.82-4.15 eV) and Fukui analysis identified the optimal site for covalent warhead installation ($f^- = 0.081$), while QM simulations revealed critical charge transfer ($0.32 e^-$) to kinase hinge regions and π -cation interactions with VEGFR2's TRP531 ($3.4 \pm 0.2 \text{ \AA}$). The developed DFT-docking-MD triad approach provided atomic-level insights into covalent binding mechanisms, validated by 100 ns simulations (RMSD < 2.0 \AA) and quantum descriptors ($\eta = 1.91$ -2.08 eV) that correlated with experimental selectivity trends. Combined with favorable ADMET properties (QPlogPo/w = 2.1, PSA = 78 \AA^2) meeting Lipinski's criteria, these findings position JR-2 as a lead candidate warranting (1) synthetic optimization through acrylamide incorporation (predicted $\Delta\Delta G = -2.3 \text{ kcal/mol}$) and solubility-enhancing modifications, and (2) immediate in vitro validation against EGFR T790M and angiogenesis models. This work not only delivers specific drug candidates but also establishes a robust computational framework for developing covalent kinase inhibitors against resistant cancers.

ACKNOWLEDGEMENTS

We express our sincere gratitude to the Department of Chemistry, University of Sahiwal, for their kind support and facilitation in providing laboratory equipment and chemicals essential for the successful completion of this research work.

AUTHOR CONTRIBUTIONS

Abdul Ghafoor and Naved Sajid performed all the experiments and prepared the main draft of the manuscript. Danish Ali and Muhammad Amir Abbas conducted the computational studies, while Hibba Asghar, Hasba Fatima, and Amina Zara Chaudhary were responsible for data validation. Javeria Rasool and Shahzaib contributed to editing and reviewing the manuscript. Amin Abid supervised the research and reviewed the manuscript outline.

CONSENT FOR PUBLICATIONS

The article does not contain any material that is offensive, defamatory, or that could, in any manner, violate the terms and conditions set forth in the agreement.

References

1. Nechak R, Bouzroua SA, Benmalek Y, Boufeoua N, Kolli BN, Martini SP, et al. Synthesis, identification and antimicrobial activity of substituted thiazolines and 1,3,4-thiadiazines from dehydroacetic acid. *Synthetic Communications*, 2019; 49:1895–905.
2. Jampilek J. Heterocycles in medicinal chemistry. *Molecules*, 2019;24(21):3839-43.
3. Santos CMM, Freitas M, Fernandes E. A comprehensive review on xanthone derivatives as α -glucosidase inhibitors. *European Journal of Medicinal Chemistry*, 2018;157:1460-79.
4. Kalaria PN, Karad SC, Raval DK. A review on diverse heterocyclic compounds as the privileged scaffolds in antimalarial drug discovery. *European Journal of Medicinal Chemistry*, 2018;158:917-36.
5. Kerru N, Bhaskaruni SVHS, Gummidi L, Maddila SN, Maddila S, Jonnalagadda SB. Recent advances in heterogeneous catalysts for the synthesis of imidazole derivatives. *Synthetic Communications*, 2019; 49(19):2437-59
6. Kerru N, Singh P, Koorbanally N, Raj R, Kumar V. Recent advances (2015-2016) in anticancer hybrids. *European Journal of Medicinal Chemistry*, 2017; 142:179-212.
7. Campanati M, Vaccari A, Piccolo O. Environment-friendly synthesis of nitrogen-containing heterocyclic compounds. *Catalysis Today*, 2000;60(3-4):289-95.
8. Vekariya RH, Patel KD, Prajapati NP, Patel HD. Phenacyl bromide: A versatile organic intermediate for the synthesis of heterocyclic compounds. *Synthetic Communications*, 2018; 48(13):1505-33.
9. Herdeiro MT, Soares S, Silva T, Roque F, Figueiras A. Impact of rosiglitazone safety alerts on oral antidiabetic sales trends: A countrywide study in Portugal. *Fundamental and Clinical Pharmacology*, 2016;30(5):440-49.
10. Singh Sidhu, J., Singla, R., & Jaitak, V. (2016). Indole derivatives as anticancer agents for breast cancer therapy: a review. *Anti-Cancer Agents in Medicinal Chemistry (Formerly Current Medicinal Chemistry-Anti-Cancer Agents)*, 16(2), 160-173.
11. Sharma, P., LaRosa, C., Antwi, J., Govindarajan, R., & Werbovetz, K. A. (2021). Imidazoles as potential anticancer agents: An update on recent studies. *Molecules*, 26(14), 4213.
12. Singh A, Patel VK, Rajak H. Appraisal of pyrrole as connecting unit in hydroxamic acid-based histone deacetylase inhibitors: synthesis, anticancer evaluation and molecular docking studies. *Journal of Molecular Structure*, 2021; 1240:130590-98.
13. Xu Z, Zhao SJ, Liu Y. 1,2,3-triazole-containing hybrids as potential anticancer agents: current developments, action mechanisms and structure-activity relationships. *European Journal of Medicinal Chemistry*, 2019;183:111700.
14. Chaudhari K, Surana S, Jain P, Patel HM. Mycobacterium tuberculosis (MTB) GyrB inhibitors: an attractive approach for developing novel drugs against TB. *European Journal of Medicinal Chemistry*, 2016; 124:160-85.
15. Sameem B, Saeedi M, Mahdavi M, Shafiee A. A review on tacrine-based scaffolds as multi-target drugs (MTDLs) for Alzheimer's disease. *European Journal of Medicinal Chemistry*, 2017; 128:332-45.
16. Akhtar J, Khan AA, Ali Z, Haider R, Shahar Yar MS. Structure-activity relationship (SAR) study and design strategies of nitrogen-containing heterocyclic moieties for their anticancer activities. *European Journal of Medicinal Chemistry*, 2017; 125:143-89.
17. Ma X, Lv X, Zhang J. Exploiting polypharmacology for improving therapeutic outcome of kinase inhibitors (KIs): an update of recent medicinal chemistry efforts. *European Journal of Medicinal Chemistry*, 2018; 143:449-63.
18. Kaur R, Dahiya L, Kumar M. Fructose-1,6-bisphosphatase inhibitors: A new valid approach for management of type 2 diabetes mellitus. *European Journal of Medicinal Chemistry*, 2017;141:473-505.
19. Patel RV, Keum YS, Park SW. Sketching the historical development of pyrimidones as the inhibitors of the HIV integrase. *European Journal of Medicinal Chemistry*, 2015; 97:649-63.

20. Walayat K, Mohsin N, Aslam S, Ahmad M. An insight into the therapeutic potential of piperazine -based anticancer activity. *Turkish Journal of Chemistry*, 2019; 43(1):1-23.
21. Delost MD, Smith DT, Anderson BJ, Njardarson JT. From oxiranes to oligomers: architectures of U.S. FDA approved pharmaceuticals containing oxygen heterocycles. *Journal of Medicinal Chemistry*, 2018; 61(24):10996-1020.
22. Bhilare NV, Auti PB, Marulkar VS, Pise VJ. Diverse thiophenes as scaffolds in anti-cancer drug development: A concise review. *Mini-Reviews in Medicinal Chemistry*, 2021; 21(2):217-32.
23. Mabkhot YN, Kaal NA, Alterary S, Al-Showiman SS, Farghaly TA, Mubarak MS. Antimicrobial activity of thiophene derivatives derived from ethyl (E)-5-(3 (dimethylamino)acryloyl)-4-methyl-2-(phenylamino)thiophene-3-carboxylate. *Chemistry Central Journal*, 2017;11(1):75
24. Zhong ZJ, Hu XT, Cheng LP, Zhang XY, Zhang Q, Zhang J. Discovery of novel thiophene derivatives as potent neuraminidase inhibitors. *European Journal of Medicinal Chemistry*, 2021; 225:113762.
25. Da Cruz RMD, Mendonça-Junior FJB, de Mélo NB, Scotti L, de Araújo RSA, de Almeida RN, Thiophene-based compounds with potential anti-inflammatory activity. *Pharmaceuticals* (Basel). 2021;14(7):692-08.
26. Available from: <https://www.cancer.gov/>.
27. Rao, S. V., O'Donoghue, M. L., Ruel, M., Rab, T., MSCAI, J., Tamis-Holland, J. E., ... & Williams, M. S. (2025). Clinical Practice Guidelines. *Circulation*, 151, e00-e00
28. Gentile, F., Jneid, H., Krieger, F. E. V., Mack, M., Rigolin, V. H., Sundt III, F. T. M., ... & Toly, C. (2021). 2020 ACC/AHA Guideline for the Management of Patients with Valvular Heart Disease. *Circulation*, 143, e00-e00
29. Nanda, J., & Bermudez, R. (2023). Imiquimod. In *StatPearls [Internet]*. StatPearls Publishing
30. Hu, C., Chen, X., Lin, X., Dai, J., & Yu, J. (2022). Raltitrexed regulates proliferation and apoptosis of HGC-27 cells by upregulating RSK4. *BMC Pharmacology and Toxicology*, 23(1), 65.
31. Hossa, K., & Małecka-Wojcieszko, E. (2025). Advances in Gastroesophageal Reflux Disease Management: Exploring the Role of Potassium-Competitive Acid Blockers and Novel Therapies. *Pharmaceuticals*, 18(5), 699.
32. Sayed, M. T. M.; Hassan, R. A.; Halim, P. A.; El-Ansary, A. K. *Recent updates on thienopyrimidine derivatives as anticancer agents. Medicinal Chemistry Research* 2023, 32, 659–681.
33. Abdelkhalek, A. S.; et al. *Synthesis of new multitarget-directed ligands containing thienopyrimidine nucleus for inhibition of 15-lipoxygenase, cyclooxygenases, and pro-inflammatory cytokines. Molecules* 2023, 28, (open access).
34. Nie, L. F., Bozorov, K., Huang, G., Zhao, J., Niu, C., & Aisa, H. A. (2018). Design, synthesis, and toward a side-ring optimization of tricyclic thieno [2, 3-d] pyrimidin-4 (3 H)-ones and their effect on melanin synthesis in murine B16 cells. *Phosphorus, Sulfur, and Silicon and the Related Elements*, 193(10), 656-667.
35. Nie, L. F., Bozorov, K., Niu, C., Huang, G., & Aisa, H. A. (2017). Synthesis and biological evaluation of novel sulfonamide derivatives of tricyclic thieno [2, 3-d] pyrimidin-4 (3 H)-ones on melanin synthesis in murine B16 cells. *Research on Chemical Intermediates*, 43(12), 6835-6843.
36. Rashad, A. E. and Ali, M.A., *Nucleosides. Nucleotides. Nucleic Acids*, 2006, vol. 25, pp. 17–28.
37. Aly, A.A., Ishak, E.A., Ramadan, M., Germoush, M.O., El-Emary, T.I., and Al-Muaiikel, N.S., *Journal of Heterocyclic Chemistry*, 2013, vol. 50, p. 451.
38. Wasfy, A.A.F., Hassan, A.A., Khattab, R.R., Abu-Zied, Kh.M., Awad, H.M., Otaibi, F.Al., and Hassan, N.A., *Research Journal of Pharmaceutical, Biological and Chemical Sciences*, 2018, vol. 9, pp. 77–88.
39. Khattab, R.R., Hassan, A.A., Kutkatd, O.M., Abuzeid, K.M., and Hassan, N.A., *Russian. Journal of General Chemistry*, 2019, vol. 89, pp. 1707–1717.
40. Hassan, A.A., Khattab, R.R., Wasfy, A.A.F., Abuzeid, Kh.M., and Hassan, N.A., *Journal of Heterocyclic Chemistry*, 2018, vol. 55, pp. 907–912.

41. Khattab, R.R., Alshamari, A.K., Hassan, A.A., Elganzory, H.H., El-Sayed, W.A., Awad, H.M., Nossier, E.S., and Hassan, N.A., *Journal of Enzyme Inhibition and Medicinal Chemistry*, 2021, vol. 36, pp. 504–516.
42. Guha M. HDAC inhibitors still need a home run, despite recent approval. *Nature Reviews Drug Discovery*, 2015;14:225–6.
43. Suraweera A, O'Byrne KJ, Richard DJ. Combination therapy with histone deacetylase inhibitors (HDACi) for the treatment of cancer: achieving the full therapeutic potential of HDACi, *Frontiers in Oncology*, 2018; 8:92.
44. Witta SE, Dziadziuszko R, Yoshida K, et al. ErbB-3 expression is associated with E-cadherin and their coexpression restores response to gefitinib in non-small-cell lung cancer (NSCLC). *Annals of Oncology*, 2009; 20:689–695.
45. Duvauchelle, V., Meffre, P. & Benfodda, Z. Green methodologies for the synthesis of 2-aminothiophene. *Environmental Chemistry Letters*. 2023;21, 597–621
46. Almutairi, S. M., Mehmood, R., Fatima, A., Ali, D., Jamal, M., Ayyaz, M., & Sarfraz, M. (2025). Chalcones from the deep: in silico medicinal chemistry and quantum chemical insights into their anticancer and anti-HIV potency. *Computational and Theoretical Chemistry*, 115380.
47. Sarfraz, M., Almutairi, S. M., Wajid, U., Imran, K., Sadia, M., Ali, D., & Elshikh, M. S. (2025). Biocompatible Deep Eutectic Solvents from Diethylammonium Chloride and Urea: Evaluation of Antioxidant Efficiency and Phytotoxicity. *ChemistrySelect*, 10(31), e03164.
48. Ali, D., Ali, M. A., Yousuf, A., & Xu, H. L. (2025). From charge transfer to sustainability: A multifaceted DFT approach to ionic liquid design. *FlatChem*, 100899.
49. Iftikhar, S., Hussain, S., Murtaza, S., Ali, D., Yousuf, S., Ali, M. A., & Refat, M. S. (2024). Synthetic route for O, S-coordinated organotin (IV) aldehydes: Spectroscopic, computational, XRD, and antibacterial studies. *Applied Organometallic Chemistry*, 38(8), e7581.
50. Ali, D., Ali, M. A., Sarfraz, M., Yousuf, A., Zulfiqar, R., Rauf, A., ... & Arshad, M. (2025). Deciphering the role of flutamide, fluorouracil, and furomollugin based ionic liquids in potent anticancer agents: Quantum chemical, medicinal, molecular docking and MD simulation studies. *Results in Chemistry*, 13, 102029.
51. Zulfiqar, R., Ali, D., Ali, M. A., Yousuf, A., Sarfraz, M., Rauf, A., & Arshad, M. (2025). Design and Prediction Physicochemical Properties of Piperazinium and Imidazolidinium Based Ionic Liquids: A DFT and Docking Studies. *Chemistry Select*, 10(18), e202405487.
52. Fields, U. A. P. (2012). MolSoft ICM Quarterly.
53. Ghafoor, A., Sajid, N., Ahmad, A., Anwar, S., Khan, M. F., Abid, A., ... & Masood, H. T. (2024). Synthesis, Characterization, and Molecular Docking Studies of Thieno [2, 3-d] pyrimidin-4 (3H)-one Derivatives. *Frontiers In Chemical Sciences*, 5(2), 25-34.
54. Ghafoor, A., Abbas, M. A., Ahmad, J., Ali, R., Abbas, M., Ahmad, A., ... & Masood, H. T. (2025). Synthesis and characterization of pyranopyrazole derivatives as potential organic nonlinear optical (NLO) materials and density functional theory (DFT) studies. *Frontiers in chemical sciences*, 6(2), 103-116.